

Microscopic mechanism of nanoscale shear bands in an energetic molecular crystal (α -RDX): A first-order structural phase transition

Sergei Izvekov¹ and Betsy M. Rice

*U.S. Army Combat Capabilities Development Command (DEVCOM) Army Research Laboratory,
Aberdeen Proving Ground, Maryland 21005, USA*

 (Received 4 April 2022; revised 2 August 2022; accepted 30 August 2022; published 22 September 2022)

Nanoscale shear bands formed in many energetic molecular crystals upon shock compression [including 1,3,5-trinitro-*s*-triazine (RDX)] are considered as a defect-free mechanism for formation and growth of hot spots which control detonation initiation. Using classical molecular dynamics, we predict the formation of similar nanoscale shear bands in the α -RDX crystal subjected to quasistatic isothermal uniaxial compression indicating a common mechanism of shear strain localization under both shock and quasistatic conditions. In the framework of the Ginzburg-Landau phenomenology coupled with the coarse-grained (CG) Helmholtz free energy of the crystal from first principles, we explore the thermodynamics of stress-induced lattice transformations under quasistatic uniaxial load. We show that the shear banding exhibits a critical behavior associated with a first-order structural phase transition with bands of localized twinning strain as transient microstructure. Analysis of the CG Helmholtz free energy suggests that the stress-induced core softening of the effective intermolecular interaction is a fundamental mechanism for a structural phase transition leading to the nanoscale shear bands.

DOI: [10.1103/PhysRevB.106.104109](https://doi.org/10.1103/PhysRevB.106.104109)

I. INTRODUCTION

Shear bands, noncrystallographic bandlike regions of localized plastic strain, are one of the most frequently observed yet least understood microstructural defects in many materials [1]. Shear localization is an important and sometimes dominant deformation underlying the constitutive plastic response in materials under high strain rate deformations [2] such as those achieved under shock-wave compression [3]. Understanding this type of plastic response is especially important for energetic molecular crystals subjected to shock loading, where shear localization is a possible “homogeneous—or *defect-free*” mechanism [4] for hot spot formation leading to explosive initiation. This possibility was explored in grain-scale crystal plasticity simulations of the pentaerythritol tetranitrate (PETN) energetic molecular crystal, which predicted adiabatic lamellar shear bands that form dynamically following shock compression [4]. More complex structural patterns of adiabatic shear bands were formed in nonequilibrium molecular dynamics (NEMD) simulations of shock-compressed 1,3,5-trinitro-*s*-triazine (alpha polymorph, α -RDX) and octahydro-1,3,5,7-tetranitro-1,3,5,7-tetrazocine (beta polymorph, β -HMX) [5,6]. These nanoscale shear bands (or nanobands [5,7]) had a crisscross pattern similar to a type of mesoscopic pattern of twins known as “tweed” [8,9] or dislocation “labyrinth” [10] structures. Using scale-bridged classical and quantum-based NEMD [11,12] and mesoscale [13] simulations, the formation and growth of hot planar nanoscale shear bands similar to those of RDX and HMX were recently observed in shocked 1,3,5-triamino-

2,4,6-trinitrobenzene (TATB) [11,12], another high-explosive molecular crystal. Atomic force microscopy of RDX shock compressed to 12.9 GPa revealed shear bands of a geometric pattern similar to that observed in the simulations [14].

The fundamental mechanism leading to the nanoscale shear banding in shocked energetic molecular crystals is unclear, even as these systems appear to share several hallmark traits of plastic strain localization. One mechanism commonly put forward to explain the plastic response in shocked solids is adiabatic shear banding due to energy dissipation within the disordered bands coupled with thermoplastic effects [15]. However, for a defect-free molecular crystal, nonequilibrium adiabatic effects do not appear to be dominant at the onset of the shear-banding transition. Instead, stress-induced structural instabilities which are governed by equilibrium thermodynamics may universally contribute to the initial shear strain localization [13,16]. There have been efforts to develop a general thermodynamic picture of shear strain localization in simpler crystalline solids with highly ordered atomistic-scale structures (e.g., metals) as well as in disordered noncrystalline systems (e.g., metallic glasses), considering the plastic deformation response as a kind of displacive (diffusive-less martensitic-type), reconstructive (diffusive) solid-solid, or coupled displacive-diffusive phase transition [7,17–24]. Descriptions of twinning as a phase transformation can be credited to the work by Ericksen [25]. Many of these efforts are relevant for the development of theories applicable to molecular crystals as well: Like metals, molecular crystals have long-range order on the unit cell scale, yet they rarely exhibit short- to intermediate-range order at the atomic scale, making them locally analogous to noncrystalline solids [26]. Molecular crystals have been shown to exhibit a range of reconstructive, martensitic, or combined stress criticality [27].

*sergiy.izvyekov.civ@army.mil

Important questions which a theory of shear strain localization in molecular crystals must address are (1) whether or not there exist basic microstructural defects/carriers similar to dislocations or deformation twinning in metals [28] or local shear transformation zones in amorphous solids [24,29] which nucleate into shear bands, and (2) whether the appearance and growth of these defects constitute a phase transition [27]. In many ordered materials, the tweed pattern is clearly a precursor of a first-order martensitic phase transition [8,30].

Here we explore the equilibrium aspects of nanoscale shear banding by considering the plastic response of α -RDX compressed quasistatically and isothermally. Using equilibrium all-atom MD simulations, we demonstrate significant similarities in the shear banding under quasistatic and shock-compression conditions. This suggests a universal mechanism of plastic instabilities in α -RDX. With very few exceptions, the instabilities associated with plastic deformation in structurally complex solids bear many of the hallmarks of a first-order (discontinuous) phase transition [23]. Hence the standard harmonic treatment applicable to second-order displacive transitions, such as in soft-phonon mode theory, is expected to fail [31]. The Ginzburg-Landau (GL) theory [32], which utilizes the concept of spatially dependent order parameters $\psi(x)$ to describe spontaneous low-symmetry distortive modes (basic microstructural defects) beyond the harmonic approximation [31], emerges as a natural theoretical framework to study first-order stress-induced criticality. Most of the applications of the GL theory to date are phenomenological, employing continuum free energy (FE) local functionals $F([\nabla\psi, \psi])$ of the phase field type [18–21,33–38] (generic mathematical forms of F such as phase field crystal models arise as the coarse-grained and continuum approximations of particle models [39]). The phenomenological approaches based on rank-one convexification of the F have been put forward in the variational reformulations [10] of an effective constitutive framework [40] which allow for certain phase decomposition (microstructures) and have been applied to study the displacive martensitic and twinning microstructures in metals [41]. One path forward to extend the GL theory toward molecular crystals while preserving a particle-based description and avoiding phenomenological assumptions is to use order parameter projected FE potentials [42] for ensembles sampled by accurate molecular simulations [43]. For a molecular crystal, the thermodynamics of lattice structure transformations is governed by the coarse-grained (CG) Helmholtz FE $A(R^N, V, T)$, the R^N -projected Helmholtz FE describing the canonical (R^N, V, T) ensemble constrained to molecular center of mass (c.m.) coordinates R^N (CG coordinates) [44]. In many cases, cooperative structural transitions are dominated by some collective distortions in the active lattice domains which are characterized macroscopically by a change in lattice symmetry such as for certain martensitic or deformation twinning transformations. These transitions can be embodied by a reduced set of bijective collective variables (order parameters) $\psi(R^N)$ allowing a GL treatment based on the generally nonlocal behavior of $A([\psi], V, T)$ in the order parameter space $[\psi(R^N), V, T]$ [45,46]. The first-principles treatment of the stress criticality can then be formulated by combining the GL phenomenology with existing bottom-up methods [44] for particle-based coarse graining suitable to

obtain accurate approximations to $A(R^N, V, T)$ from micro-simulations [47].

We formulate a general GL theory of first-order stress-induced nanoscale shear banding by coupling the GL phenomenology with the $A(R^N, V, T)$ derived from first principles (all-atom MD simulations) using the force-matching based multiscale coarse-graining (MSCG/FM) approach [44,48–52] and extending the formalism to the Gibbs ensemble (Sec. II). We then apply the formalism to investigate the fundamental structural instability leading to nanoscale shear banding in α -RDX (Sec. III). Based on our analysis of MD isothermal simulations of α -RDX under [100] uniaxial compression, we suggest that the genesis of the nanoscale shear banding is the shear localization through activation of the deformation twinning modes [12,13,53]. Using GL calculations in which $\psi(R^N)$ describes the progress of deformation twinning, we show that the shear banding in uniaxially stressed α -RDX clearly displays the signature of a first-order (discontinuous) phase transition. The discontinuous nature of the shear localization complicates the observation of transient microstructure of localized twinning shear preceding the disordered, reconstructed shear-band microstructure. One prominent change observed at the onset of the plastic regime is a sudden core softening (core collapse) of the effective intermolecular interaction (as described by the CG Helmholtz FE functional) which we link to stress-induced molecular deformations. Core-softened interactions [54–56] are known to lead to novel criticality and complex phase behavior in both model [57,58] and real condensed matter systems [59]. We hypothesize that the nanoscale shear banding is one of these types of criticality in molecular solids composed of flexible molecules.

II. THEORY

A. CG Helmholtz free energy potential

We consider a N -molecule supercell of a classical monomolecular crystal formed from n atoms with masses $\{m_i\}_{i=1}^n$. The dynamics of the crystal is governed by the Hamiltonian $H(r^n, p^n) = T^{\text{atm}}(p^n) + u^{\text{atm}}(r^n)$ where $r^n \equiv \{r_i\}_{i=1}^n$ are atomic position coordinates, $p^n \equiv \{p_i\}_{i=1}^n$ are conjugate momenta, $T^{\text{atm}}(p^n) = 0.5 \sum_i m_i^{-1} p_i^2$ is the total kinetic energy, and $u^{\text{atm}}(r^n)$ is the interaction potential. The CG coordinates (order parameters) suitable to describe a range of lattice structure phases are molecular c.m. positions, $R^N \equiv \{R_I\}_{I=1}^N$,

$$R_I(r^n) = M^{-1} \sum_{i \in I} m_i r_i, \quad (1)$$

where M is the molecular mass. The conjugate momenta $P^N \equiv \{P_I\}_{I=1}^N$ and generalized forces $F^N \equiv \{F_I\}_{I=1}^N = \{\dot{P}_I\}_{I=1}^N$ are, respectively,

$$P_I(p^n) = \sum_{i \in I} p_i, F_I(r^n) = \sum_{i \in I} f_i, \quad (2)$$

where $\{f_i\}_{i=1}^n \equiv f^n$ are the atomistic forces. The coordinates (R^N, P^N) are a subset of the canonical Jacobi coordinates [60] $(R^N, P^N, \xi^N, p_\xi^N)$ with ξ^N, p_ξ^N describing the intramolecular positional and momentum degrees of freedom (d.f.). The

phase space (R^N, P^N) can be viewed as that of the equivalent CG ensemble [49]. We consider an extended set of thermodynamic state variables (R^N, V, T) . The canonical distribution function of the ensemble at fixed (R^N, V, T) is the following conditional probability density [43],

$$f_{R^N}(r^n, p^n) = Z_{R^N}^{-1} \delta[R^N(r^n) - R^N] e^{-\beta H(r^n, p^n)}$$

$$\text{with } Z_{R^N} = h^{-3n} g(n)^{-1} \int dr^n dp^n \delta[R^N(r^n) - R^N] e^{-\beta H(r^n, p^n)}, \quad (3)$$

where $g(n)$ is an atomic configuration degeneracy. The statistical thermodynamics of the (R^N, V, T) ensemble is determined by the conditional CG Helmholtz FE, $A = -\beta^{-1} \ln Z_{R^N}$, which takes the form

$$A(R^N, V, T) = A_{id}^{CG}(V, T) + A_{id}^{intra}(V, T) + A_c(R^N, V, T). \quad (4)$$

Here,

$$A_{id}^{CG}(V, T) = -\beta^{-1} \ln h^{-3N} N!^{-1} V^N \int dP^N e^{-\beta T^{CG}(P^N)},$$

$$A_{id}^{intra}(V, T) = -\beta^{-1} \ln h^{-3(n-N)} g_\xi^{-1} V^{n-N} \int dp_\xi^N e^{-\beta T^{intra}(p_\xi^N)}, \quad (5)$$

are, respectively, the CG and intramolecular ideal gas contributions and

$$A_c(R^N, V, T) = -\beta^{-1} \ln V^{-n} \int dr^n \delta[R^N(r^n) - R^N] \times e^{-\beta u^{atm}(r^n)}$$

$$= -\beta^{-1} \ln V^{-n+N} \int d\xi^N e^{-\beta u^{atm}(R^N, \xi^N)} \quad (6)$$

is the configurational FE. In Eq. (5), $T^{CG}(P^N) = (2M)^{-1} \sum_I P_I^2$ and $T^{intra}(p_\xi^N)$ are, respectively, the total translational (CG) and internal kinetic energies of the molecules [$T^{atm}(p^n) = T^{CG}(P^N) + T^{intra}(p_\xi^N)$], and g_ξ is a configurational degeneracy of the intramolecular d.f. In Eq. (6), we redefine $u^{atm}(r^n)$ in the new coordinates as $u^{atm}(R^N, \xi^N) \equiv u^{atm}[r^n(R^N, \xi^N)]$. The expectation of the observable $O(r^n, p^n)$ in the (R^N, V, T) ensemble is the following conditional expectation: $\langle O \rangle_{R^N} = \int dr^n dp^n f_{R^N} O$. For a bijective function $\psi(R^N)$, we obviously have $\langle \psi \rangle_{R^N} = \psi$, and therefore coarse-grained lattice order parameters of lower resolution can be constructed as bijective mappings of the R^N .

B. MSCG/FM method and dependency on the particle density

The MSCG/FM method [44,47,49,50,52,61] provides least-squares approximations to the following thermodynamic forces:

$$\langle F_I \rangle_{R^N} = -\nabla_{R_I} A(R^N, V, T), \quad P_c = -\frac{\partial}{\partial V} (A_c + A_{id}^{intra}). \quad (7)$$

Here,

$$\langle F_I \rangle_{R^N} = \frac{\int dr^n e^{-\beta u^{atm}(r^n)} \delta[R^N(r^n) - R^N] F_I(r^n)}{\int dr^n e^{-\beta u^{atm}(r^n)} \delta[R^N(r^n) - R^N]} \quad (8)$$

is a conditional thermodynamic expectation of $F_I(r^n)$ given R^N , and P_c is the thermodynamic pressure from the configurational and intramolecular momentum d.f. Within the MSCG/FM approach, the force $\langle F_I \rangle_{R^N}$, which is a mean force experienced by the CG coordinates [62–64], is approximated by a central and pairwise additive force:

$$\langle F_I \rangle_{R^N} \approx F_I^{2b}(R^N) = \sum_{J \neq I} f^{2b}(R_{IJ}, \alpha) n_{IJ}, \quad (9)$$

where $f^{2b}(R, \alpha) = a_k(R) f_k^{2b} + b_k(R) f_{k+1}^{2b} + c_k(R) f_k^{2b''} + d_k(R) f_{k+1}^{2b''}$, $R_k < R \leq R_{k+1}$, is a cubic spline defined on a distance grid $\{R_k\}_{k=1}^{K_{bin}}$ (the coefficients a_k, b_k, c_k, d_k are known rational functions of R, R_k, R_{k+1}). The set $\alpha = \{f_k^{2b}, f_k^{2b''}\}_{k=1}^{K_{bin}}$ is selected as the adjustable parameter set. The optimal set $\alpha = \alpha_{min}$ is determined by minimizing the objective function,

$$\chi^2(\alpha) = \left\langle N^{-1} \sum_{I=1}^N \left| F_I(r^n) - \sum_{J \neq I} f^{2b}(R_{IJ}, \alpha) n_{IJ} \right|^2 \right\rangle + \left\langle \left| P_c(r^n, p_\xi^N) - (3V)^{-1} \sum_{I < J} f^{2b}(R_{IJ}, \alpha) R_{IJ} \right|^2 \right\rangle, \quad (10)$$

where P_c is the instantaneous virial pressure: $P_c = \langle P_c \rangle$. The second term in Eq. (10) is equal to $\langle |\mathcal{P}^{atm}(r^n, p^n) - \mathcal{P}^{CG}(R^N, P^N)|^2 \rangle$ where \mathcal{P}^{atm} and $\mathcal{P}^{CG} = (3V)^{-1} [2T^{CG}(P^N) + \sum_{I < J} f^{2b}(R_{IJ}, \alpha) R_{IJ}]$ are instantaneous atomistic and CG virial pressures, respectively. This term implements a pressure constraint [50,65,66] which allows one to correctly predict the atomistic thermodynamic pressure $P^{atm} = \langle \mathcal{P}^{atm} \rangle$ in the CG simulations. The force f^{2b} at α_{min} becomes a function of V, T : $f^{2b}(R_{IJ}, V, T)$. We can write the following pairwise additive approximation,

$$A(R^N, V, T) \approx A^{2b}(R^N, V, T) = \sum_{I < J} u^{2b}(R_{IJ}, V, T) + A_0(V, T) + A_{id}^{CG}(V, T), \quad (11)$$

where $u^{2b}(R_{IJ}, V, T) = \int_{R_{IJ}}^{R_{cut}} dR f^{2b}(R, V, T)$ and $A_0(V, T)$ is the potential which includes $A_{id}^{intra}(V, T)$.

The approximation equation (11) may not be transferrable to nonuniform systems [50,67], but this deficiency can be alleviated by considering the A as a functional of local particle density ρ : $A(R^N, [\rho], T)$. For MSCG/FM models, the local ρ dependency is first introduced into the force $f^{2b}(R_{IJ}, [\rho]) = f^{2b}(R_{IJ}, \{\rho_I\}_{I=1}^N)$, where

$$\rho_I = \sum_{J \neq I} \omega_\rho(R_{IJ}) \quad (12)$$

is the local density of CG particles located at R_I [68]. The pair-additive characteristic of $\nabla_{R_I} A$ and A is maintained with the two-point approximation:

$$f^{2b}(R_{IJ}, \{\rho_I\}_{I=1}^N, T) \approx f^{2b}(R_{IJ}, \rho_I, \rho_J, T) = 0.5[f^{2b}(R_{IJ}, \rho_I, T) + f^{2b}(R_{IJ}, \rho_J, T)]. \quad (13)$$

Following Refs. [66,67], the forces f^{2b} are individually parametrized on a preselected grid of reference densities $\{\rho_i\}$:

$$f^{2b}(R_{IJ}, \rho, T) = (1 - a_\rho) f^{2b}(R_{IJ}, \rho_i, T) + a_\rho f^{2b}(R_{IJ}, \rho_{i+1}, T),$$

where $a_\rho = (\rho - \rho_i)(\rho_{i+1} - \rho_i)^{-1}$,
 $\rho_i \leq \rho < \rho_{i+1}$. (14)

Equation (11) cannot be applied directly to calculate the A^{2b} as the potential A_0 is not available. The following relation,

$$A(R^N, V, T) \approx A^{2b}(R^N, \{\rho_I\}_{I=1}^N, T) = \sum_{I < J} \int_{R_{IJ}}^{R_{cut}} dR'_{IJ} \times f^{2b}[R'_{IJ}, \rho_I R_{IJ}^3 R_{IJ}'^{-3}, \rho_J R_{IJ}^3 R_{IJ}'^{-3}, T] + A_{id}^{CG}(V, T),$$
 (15)

can be used to evaluate A^{2b} numerically [51,52,66], assuming that the work by F_I^{2b} is path independent.

C. Formulation in terms of CG Helmholtz and Gibbs free energies

The CG internal energy $E(R^N)$ and the CG entropy $S(R^N)$ can be introduced via a standard thermodynamic relation: $A(R^N) = E(R^N) - TS(R^N)$. The CG thermodynamics then becomes

$$dA(R^N, V, T) = - \sum_I \langle F_I \rangle_{R^N} dR_I - P_{id}^{CG} dV - S(R^N) dT, \quad (16)$$

where $P_{id}^{CG} = -(\partial A_{id}^{CG} / \partial V)_{R^N, T}$ is the ideal gas contribution to P^{CG} . The MSCG/FM procedure with the pressure constraints leads to the pressure P_c [Eq. (7)] being effectively included into $\{\langle F_I \rangle_{R^N}\}_{I=1}^N$. Assuming Cauchy-Born kinematics (locally uniform deformation of R^N), we transform $\sum_I \langle F_I \rangle_{R^N} dR_I = V_\Omega \sum_I \hat{\sigma}_I : d\hat{\epsilon}_I$ where $\hat{\sigma}_I$ is the local Cauchy stress; $\hat{\epsilon}_I = 0.5(\hat{F}_I^{-T} \hat{F}_I^{-1} - \hat{I})$ is the conjugate Almansi strain from the discrete deformation gradient $\hat{F}_I = \nabla_{R_I} R'_I$ of the deformed lattice R^N . Formulations by Hardy [69], $\hat{\sigma}_I = \hat{\sigma}^H(R_I)$, or by Lutsko [70], $\hat{\sigma}_I = \hat{\sigma}_I^L$ with averaging volume V_Ω , can be used; in our work, we used the Lutsko formulation. We have $P^{atm} = (3V)^{-1} V_\Omega \text{Tr}(\sum_I \hat{\sigma}_I) + P_{id}^{CG}$.

The Gibbs FE formulation is obtained from Eq. (16) which can be written as $dA = -V_\Omega \sum_I \hat{\sigma}_I : d\hat{\epsilon}_I - P_{id}^{CG} dV - S dT$ using the Legendre transformation with respect to $\{\hat{\sigma}_I\}_{I=1}^N$ and P_{id}^{CG} . The resulting CG Gibbs FE is

$$G(\{\hat{\sigma}_I\}_{I=1}^N, P_{id}^{CG}, T) = A + V_\Omega \sum_I \hat{\sigma}_I : \hat{\epsilon}_I + P_{id}^{CG} V. \quad (17)$$

A discontinuity in any of the variables $\{\hat{\sigma}_I\}_{I=1}^N, P_{id}^{CG}$ may indicate a stress-induced phase transition. For convenience, we reduce the dimensionality of the stress field variable space by assuming that the mechanical energy of the system uniaxially deformed along \vec{n} can be written as $V_\Omega \sum_I \hat{\sigma}_I : \hat{\epsilon}_I + P_{id}^{CG} V = V \hat{\sigma} : \hat{\epsilon}$ where $\hat{\sigma} = \sigma \vec{n} \otimes \vec{n}$ is the external Cauchy stress imposed by the NsT barostat (acting in the \vec{n} direction only)

and $\hat{\epsilon}$ is the effective Almansi strain. This yields the following representation of the Gibbs FE: $G(\hat{\sigma}, T) = A + V \hat{\sigma} : \hat{\epsilon}$. For the uniaxial compression studied in this work, we have $\vec{n} = [100]$ and $\sigma = \sigma_{xx}$. To observe a structural transition at critical $\hat{\sigma}$ in the compression simulations, thermal fluctuations must be introduced into the dynamics of R^N . This is achieved by coupling the atomistic (and hence R^N) dynamics using the anisotropic Melchionna-Nosé-Hoover barostat [71,72] which controls the $\hat{\sigma}$.

D. Ginzburg-Landau treatment of shear strain localization

We will develop a single order parameter theory of the shear strain localization based on the following assumptions: (1) The deformed lattice R^N can be assigned the plastic order parameter $\psi(R^N)$ which describes the degree of localized shear deformation with $\psi = 0$ corresponding to the unsheared R^N ; (2) the shear banding is described by cooperative modes that are bijective and linear functions of ψ : $\delta R^N(\psi) \equiv \{\delta R_I(\psi)\}_{I=1}^N$. For example, our observations (discussed below) indicate that in α -RDX, the shear bands are initiated as bands of localized twinning strain with simple shear deformation modes $\delta R_I = [\hat{F}^P(\gamma) - \hat{I}]R_I$, where $\hat{F}^P(\gamma) = \hat{I} + \gamma \vec{s} \otimes \vec{n}$, in the shear-band regions (S phase), and complementary deformation modes $\delta R_I = [\hat{F}^P(-\gamma) - \hat{I}]R_I$, $\gamma_P \gamma^{-1} = \text{const}$, in the parent crystal (P phase). In this picture the structural instability can be described by an order parameter $\psi = \gamma$.

Following the nonlinear GL phenomenology, the FE change above the structural phase transition is an analytic function of the order parameter:

$$\Delta A(\psi) = \psi^2 \Delta A_{\psi^2} + \psi^3 \Delta A_{\psi^3} + \psi^4 \Delta A_{\psi^4} + o(\psi^4), \quad (18)$$

$$\Delta A_{\psi^n} = \frac{1}{n!} \sum_{I_1, \dots, I_n} \frac{\partial^n \Delta A}{\partial R_{I_1} \cdots \partial R_{I_n}} \partial_{\psi} \delta R_{I_1} \cdots \partial_{\psi} \delta R_{I_n},$$

$$\frac{\partial^n \Delta A}{\partial R_{I_1} \cdots \partial R_{I_n}} = - \frac{\partial^{n-1} \langle F_{I_1}(r^n) \rangle_{R^N}}{\partial R_{I_2} \cdots \partial R_{I_n}}. \quad (19)$$

For simple shear deformation modes, we have $\partial_{\psi} \delta R_{I \in S} = \vec{s} \otimes \vec{n}$, $\partial_{\psi} \delta R_{I \in P} = -\text{const} \times \vec{s} \otimes \vec{n}$. The structural equilibrium condition is $\Delta A_{\psi} = 0$ or $\{\partial \Delta A / \partial R_I\}_{I=1}^N = 0$. At $\hat{\sigma} > \hat{\sigma}^c$, where $\hat{\sigma}^c$ is the critical (plastic yield) stress, the equilibrium structure is a solution of $\partial \Delta A / \partial \psi = 0$, $\Delta A_{\psi^4} > 0$. If an invariant $\Delta A_{\psi^3} \neq 0$ then there are two solutions $\psi \neq 0$ which are first-order (discontinuous) localizations of twinning strain at $\hat{\sigma}^c$. For a first-order instability, the solutions $\psi \neq 0$ are not infinitesimally small. Thus, in crystals such as α -RDX in which the deformation twinning modes are hard to activate, these bands of localized twinning shear may exist as transient defects which appear at the onset of the phase transition. Subsequently, they become reconstructed or disordered, eventually transforming into shear bands. The type of the structural phase transition is determined by the invariance of $\Delta A(\psi)$ under inversion $\psi \rightarrow -\psi$ and hence by the symmetry of the parent crystal and the crystallographic orientations of the twinning shear bands.

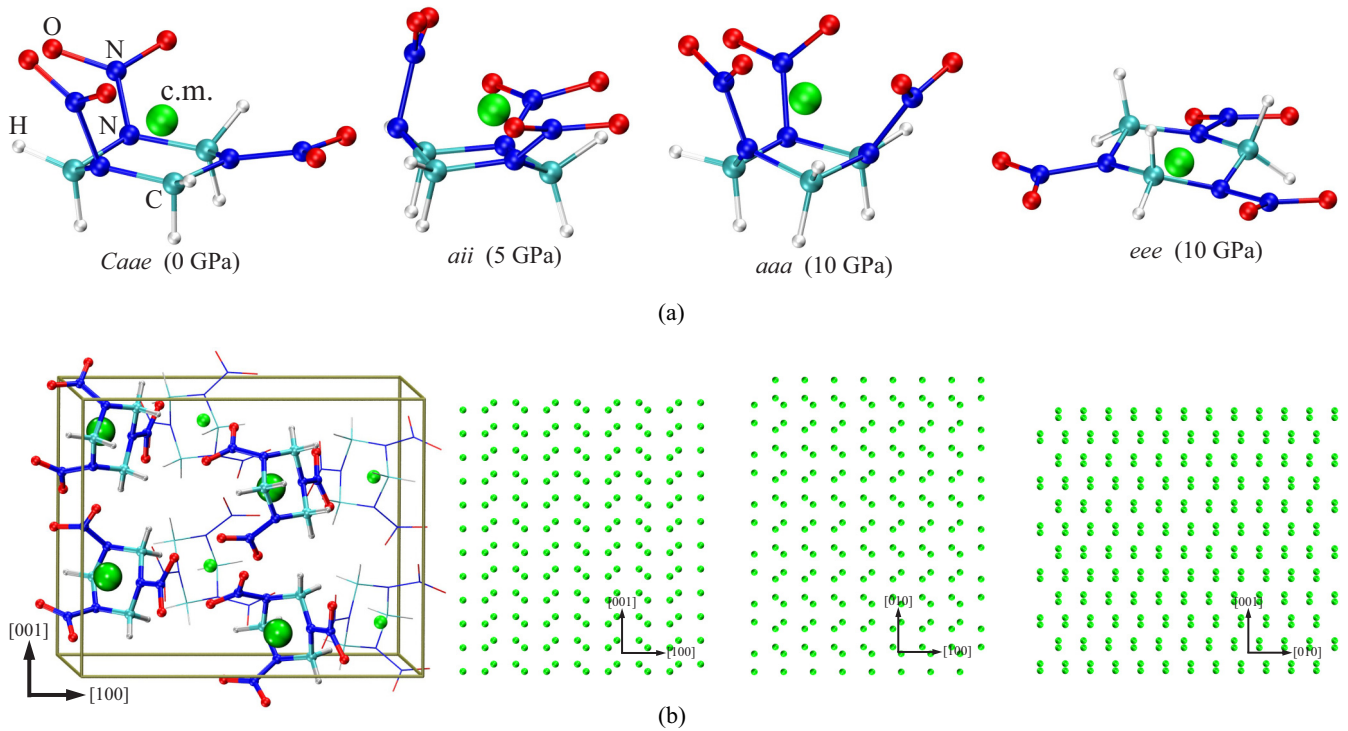


FIG. 1. (a) α -RDX molecule (*Caae* conformation) and its coarse graining with the green ball denoting the location of the molecular c.m., along with other state-dependent conformers. (b) α -RDX crystal at standard ambient conditions. The box outlines the unit cell with eight molecules; the green balls in each are the molecular c.m. The skeletons and c.m. spheres of the four molecules in the front are enlarged. Three views of the R^N lattice are shown on the right.

III. RESULTS

We first describe atomistic simulations followed by presenting relevant results, some of which are discussed in [52], on the plastic deformation in the atomistic simulations. The remaining sections formulate the GL theory of shear banding.

A. Atomistic simulations

The RDX molecule has numerous conformations that are thermodynamic state and phase dependent. The ring of the RDX molecule may adopt a chair (*C*), twist (*T*), or boat (*B*) conformation. The angles which the NO_2 groups form with the normal of the ring range from 10° to 170° . The NO_2 group conformations with the angles closer to 90° are called pseudoequatorial (*e*), those with the angles smaller than 45° are referred to as axial (*a*) conformations, and the conformations with the angles within the intermediate range are sometimes labeled as (*i*) [52,73,74]. Previous experimental and computational studies have indicated the conformational isomerism of RDX molecules with the existence of *aaa*, *aae*, *ae*, and *eee* conformers [75–79] as depicted in Fig. 1(a). Infrared spectroscopy studies [75] have shown the existence of the *aaa* and *eee* conformers in every phase except the α -RDX polymorph while more recent studies [73,80] have identified the *aae* and *aaa* as ground states for the molecules in α -RDX and β -RDX, respectively. In α -RDX, defects or deformation may lead to a population of an additional conformation state (*ae*) [81]. The *aii* conformers were observed in isostatic [100] compression simulations [52,74]. Under standard am-

bient conditions, RDX crystallizes in the orthorhombic space group *Pbca* and eight molecules per unit cell (α -RDX polymorph). Figure 1(b) shows the α -RDX unit cell in atomistic and molecular c.m. coordinates as well as the lattice R^N . Three slip systems in α -RDX monocrystals were identified from quasistatic loading and nanoindentation experiments [82,83], and confirmed by atomistic [84,85] and CG simulations [86]: $(021)[100]$, $(0\bar{2}1)[100]$, $(011)[100]$, $(0\bar{1}1)[100]$, $(010)[100]$, $(010)[001]$ with critical resolved stress within 0.6–1 GPa.

The atomistic classical force field published by Smith and Bharadwaj [87,88] has shown outstanding predictive capability for modeling a variety of nonreactive properties in RDX [84,89–91], and has been used in isothermal compression simulations [52,91]. In [52], the compression simulations employed oblong cells of two sizes: the “Large” cell (L cell) measuring $120a \times 6b \times 21c$, containing 120 960 molecules, the “Small” cell (S cell) measuring $20a \times 6b \times 6c$, containing 5760 molecules, and a smaller cell (s cell) measuring $2a \times 3b \times 3c$. A stress σ_{xx} was applied in the [100] direction, while the dimensions in the [010] and [001] directions were kept constant to produce the engineering strain-stress curve. The supercells were compressed isothermally at 300 K using the following protocol: The target σ_{xx} was increased with an increment of 1 GPa, the *NsT* run for the new target σ_{xx} was initiated from the final configuration of the previous σ_{xx} run, and the system was simulated for 500 ps to achieve a compression corresponding to the target σ_{xx} . This protocol led to strain rates on the order of 10^8 s^{-1} which are comparable to those achieved in the experiments, although considered as high [92].

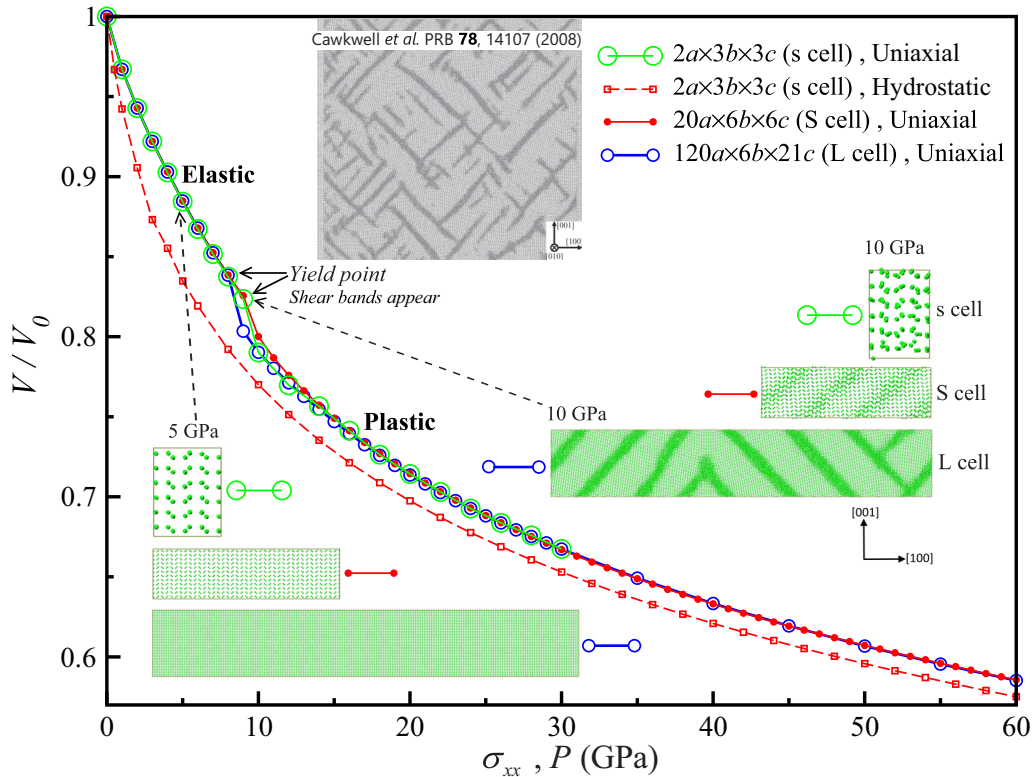


FIG. 2. [100] uniaxial engineering strain-stress and hydrostatic strain-pressure curves for the different cell sizes of α -RDX [52]. The gray-scale image at the upper portion of the figure is from Ref. [93] and shows the labyrinthlike shear-band structure of the R^N projected α -RDX cell (dimensions $141a \times 3b \times 141c$) following the propagation of a planar shock wave along [100] with a pressure of 7.9 GPa. The remaining images show the [010] view of the R^N projections of the cells [100] compressed to 5 GPa (elastic regime) and 10 GPa (plastic regime).

Nevertheless, these strain rates are lower than those observed under shock compression. For example, in [90] the maximum strain rate in shocked RDX with a particle velocity of 1 km/s is $3\text{--}5 \times 10^{11} \text{ s}^{-1}$. Work by Munday *et al.* demonstrated that applied strain rates higher than those used in the current study are quasistatic for α -RDX [84,91].

B. Plastic deformation

Figure 2 shows the engineering strain-stress curves under [100] loading [52]. The strain-stress curve is markedly insensitive to the cell size, and exhibits a yield point σ_{xx}^c [90,93] within 9–10 GPa [52]. The plastic deformation in both the S and the L cells is characterized by a shear localization within the bands, which are clearly visible in the R^N projection of the atomistic cells [Figs. 2, 3, 4, and 5(a)]. The shear bands have nearly uniform thickness, and are not aligned with any preferable crystallographic direction. The bands propagate at $\alpha = 45^\circ$ to [100] and lie in the [010] zone. In the S cell, the striped pattern of alternating S and P bands forms [Figs. 2, 3, and 5(a)]: The S slabs of inelastically sheared crystal are confined between two plane parallel surfaces (denoted as “twinning” planes). The time resolved initiation of shear banding [Fig. 5(a)] points to the onset of deformation twinning through localization of simple shear deformation as the fundamental structural instability. The elastically deformed P regions undergo simple shear deformation in the opposite direction which resembles a [010] rotation due to an insignif-

icant pure shear component in the polar decomposition (see Sec. III C). Due to variations in molecular conformations [52], the effective intermolecular interaction within the S and P domains of R^N may differ [the difference is captured by the ρ -dependent $f^{2b}(R, \rho, T)$] and therefore the twinning strain [53] at which the sheared and parent phases of R^N are structurally equivalent (rotation or reflection twins) may not be reached. As we discussed in [52], the shear bands are not formed in the s cell (10 GPa snapshot in Fig. 2); however, at σ_{xx}^c , abrupt molecular conformational changes occur through the whole of the cell (similar to that seen within the atomistic shear band in Fig. 3). This suggests that a distinct plastic response may be due to the modification of the effective intermolecular interaction $u^{2b}(R)$ [Eq. (11)] caused by stress-induced changes in the statistics of molecular conformers. In the S cell, the geometrical pattern of the shear bands does not change upon use of tenfold higher strain rates. Conversely, as evident from Fig. 4, the pattern of shear bands in the L cell compressed at higher strain rates evolves toward more abundant crossings and becomes similar to the tweed or labyrinth patterns observed in shock-compression simulations [5,52,74,90,93,94] (see Fig. 2).

C. Plastic order parameter

The structural phase transition in the [100]-compressed S cell, in which shear bands propagate through the periodic boundaries adopting a lamellar S – P arrangement (Figs. 2 and

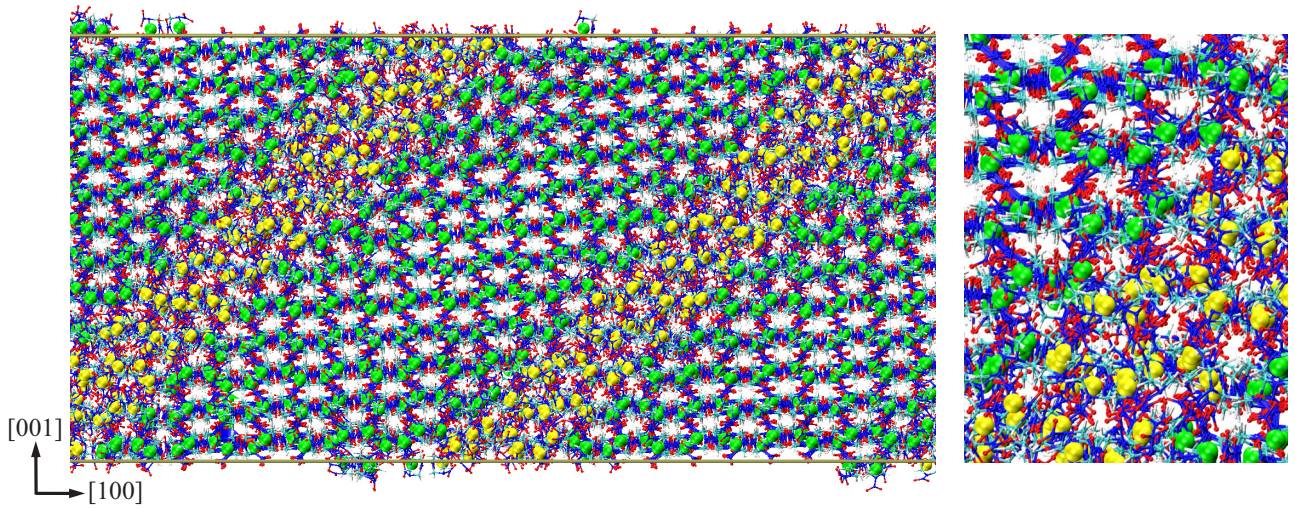


FIG. 3. Left: [010] view of superimposed atomistic and R^N structures of the shear-banded S cell at $\sigma_{xx} = 10$ GPa. The R^N are shown as large spheres, colored green in the parent region and yellow in the shear-band region. Right: Magnification of part of the S cell shown to the left.

3), can be studied using the single order parameter formulation of the GL theory. From examining Fig. 5(a), we conclude that the twinning planes lie in the [010] zone, are deformation invariants, and upon deformation translate homogeneously in the opposite directions $\pm \vec{s} \perp [010]$ ($\{101\}\langle 10\bar{1}\rangle$ and $\{101\}\langle 101\rangle$ twin variants). This is possible only if the deformation modes of the S and P domains are simple shears (respectively): $F^P(\gamma) = (\hat{I} + \gamma \vec{s} \otimes \vec{n})$, $F^P(-\gamma_P) = (\hat{I} - \gamma_P \vec{s} \otimes \vec{n})$. The polar decomposition $F^P = R^T U$ holds for both S and P domains with pure [010] rotations $R(\varphi)$ by $\phi = \tan^{-1} \gamma/2$, $\phi_P = -\tan^{-1} \gamma_P/2$, respectively. In the P band, the stretch U is insignificant due to large L_P and the deformation is close to $R(\varphi_P)$ (Fig. 5). The compatibility requirement that the twinning interface be coherent necessitates that Hadamard jump condition applies [95],

$$\gamma = \gamma_P \frac{L_P}{L_S}, \quad (20)$$

where L_S and L_P ($L_S < L_P$) are (respectively) the thickness of the shear band and parent phase regions [Fig. 5(b)]. If the L_S , L_P are the same across all bands (as observed), then the

deformed R^N and hence $A(R^N, V, T)$ become unique functions of γ , which we choose as the plastic order parameter $\psi \equiv \gamma(R^N)$. For bigger cells, the lamellar arrangement of shear bands may evolve toward the tweed- or labyrinthlike patterns [9,10] of a lower translational symmetry which are composed of coexisting plastically deformed S_1-P_1 , S_2-P_2 domains with two different competing orientations $s_1 \perp s_2$ of S bands [93] (Figs. 2 and 4). This would require the two order parameter theory [33] with $\psi_i(R^{N_i} \in S_i - P_i)$, $i = 1, 2$ in which the pattern and phase diagram are determined by behavior of $A(R^N, V, T)$ in the (ψ_1, ψ_2, V, T) space. In the S cell, the requirement equation (20) leads to the following additive representation: $\Delta A_{\gamma^n} = \Delta A_{\gamma^n}|_S + \Delta A_{\gamma^n}|_P L_S^n L_P^{-n}$. Under uniaxial compression, the crystal loses stability toward twinning strain localization at the earliest occurrence of the conditions $\Delta A_{\gamma}|_S + \Delta A_{\gamma}|_P L_S L_P^{-1} = 0$, $\Delta A_{\gamma^2}|_S + \Delta A_{\gamma^2}|_P L_S^2 L_P^{-2} < 0$, which prescribe a relative size $L_S L_P^{-1}$ of the S and P phase domains. Since the inversion $\vec{s} = -\vec{s}$ is not associated with any symmetry element of the $Pbca$ space group, the $A_{\gamma^3} \neq 0$ is not prohibited by the crystal symmetry and thus

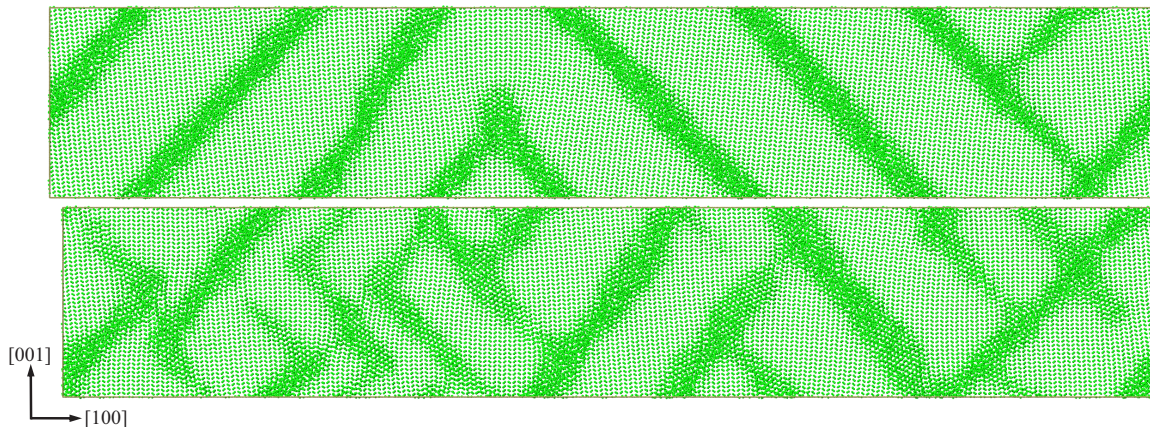


FIG. 4. R^N structure of the L cell at $\sigma_{xx} = 9$ GPa under quasistatic (upper) and high strain rate (bottom) compressions.

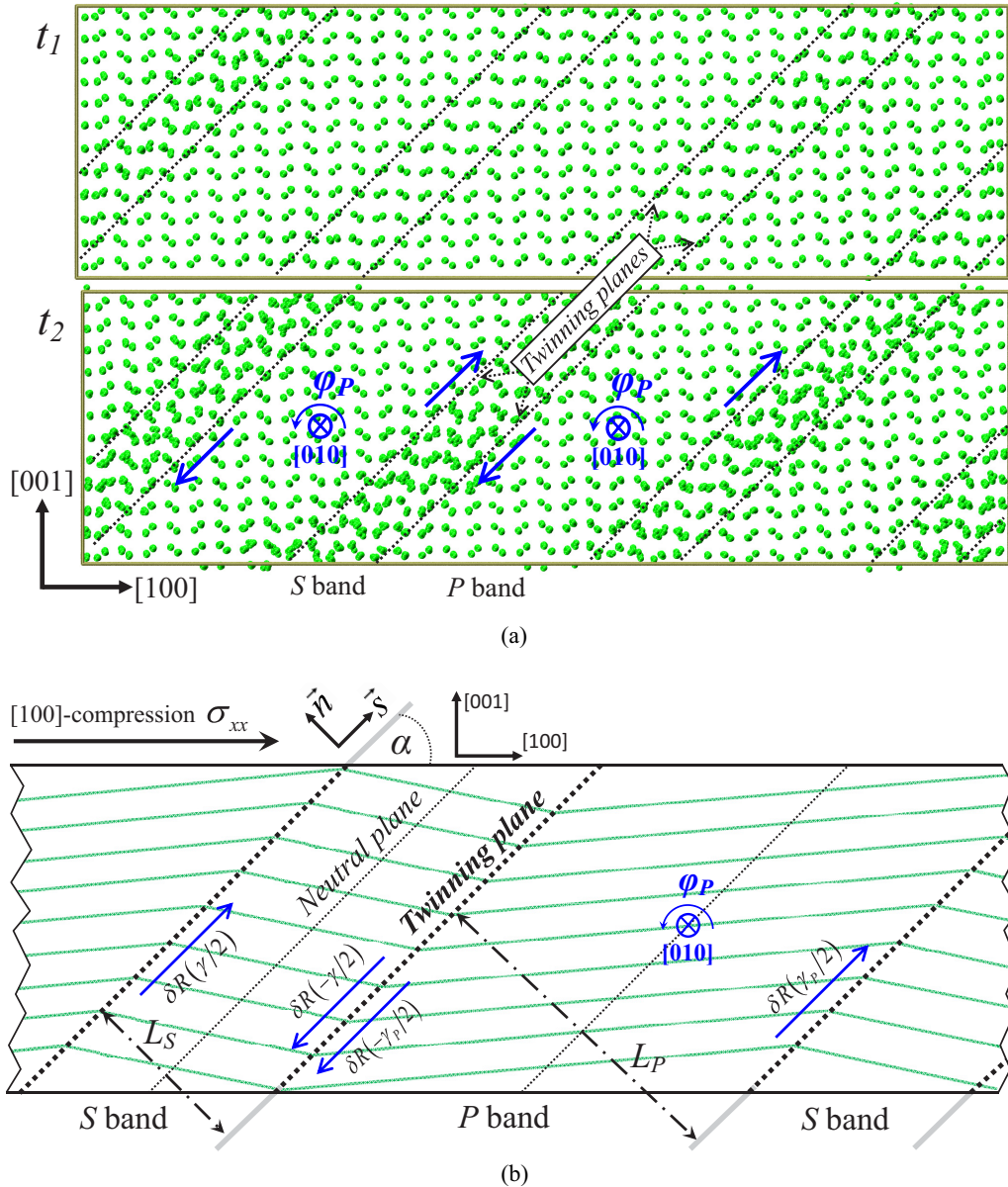


FIG. 5. The nonsymmorphic deformation twinning mechanism of shear banding in the R^N representation. (a) Snapshots correspond to two sequential configurations ($t_2 > t_1 > 0$) from a MD simulation of the S cell [100] compressed to $\sigma_{xx} = 10$ GPa at quasistatic strain rates showing the early stage of shear banding. Blue arrows outline the major deformation modes: directions of simple shears in the shear (S) and parent crystal (P) bands and pure [010] rotation component $R(\varphi_P)$ of the deformation in the P bands (see Sec. III C). (b) Order parameter $\psi \equiv \gamma(R^N)$ describing the progress toward deformation twinning under uniaxial σ_{xx} . Deformations in the S and P bands are simple shears δR_I with (respectively) γ , γ_P related by Eq. (20) and in opposite directions $\pm \vec{s}$ as shown by the arrows.

the shear banding in α -RDX may constitute a first-order phase transition. For molecular crystals having lattices of higher symmetry, the shear banding may become a second-order phase transition [35].

D. Calculation of $A(R^N, V, T)$

The thermodynamic force $-\nabla_{R^N} A(R^N, V, T)$ and its (Helmholtz FE) potential $A(R^N, V, T)$ were obtained using the MSCG/FM method as described in Sec III. The reference data for the MSCG/FM procedure were sampled from a series of MD simulations of the s cell subjected to [100] uniax-

ial compression to stresses $\{\sigma_k\} = \{0, 5, 8, 9, 10, 15, 20 \text{ GPa}\}$. The cell was first compressed quasistatically and isothermally [84,91], $T = 300$ K, to the target σ_k . Subsequently, for each σ_k , the trajectories $r^n(t)$, $f^n(t)$ were recorded at 0.2 ps intervals during the 30 ps of NVT simulations initiated from the final configuration of the compression run. The r^n , f^n were then transformed into R^N , F^N [Eqs. (1) and (2)] and tagged with the corresponding instantaneous T^{CG} , \mathcal{P}^{atm} . The splines f^{2b} are defined on a grid with $R_{\text{cut}} = 16 \text{ \AA}$. The objective function χ^2 in Eq. (10) was minimized over the sampled $R^N(t)$ as described in Refs. [51,66]. For nonhomogeneously deformed R^N , we used the ρ dependency implemented in accordance

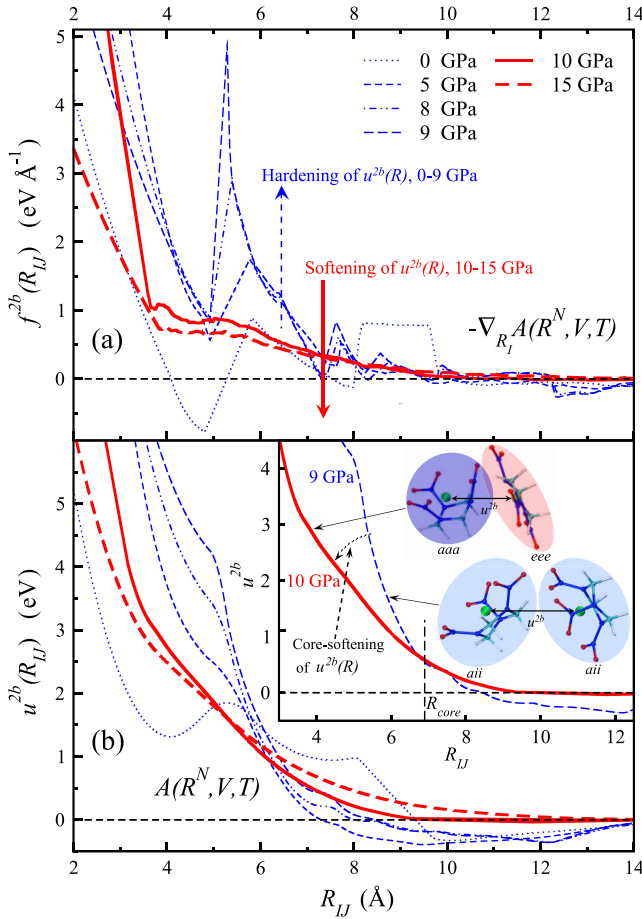


FIG. 6. (a) MSCG/FM terms $f^{2b}(R_{IJ})$ in $-\nabla_{R_I} A(R^N, V, T)$ [Eq. (9)] at different σ_{xx} . (b) Corresponding terms $u^{2b}(R_{IJ})$ in $A(R^N, V, T)$ [Eq. (11)]. Vertical arrows indicate stiffening of $-\nabla_{R_I} A(R^N, V, T)$ with increasing σ_{xx} from 0 to 9 GPa (dashed blue arrow) followed by the $-\nabla_{R_I} A(R^N, V, T)$ softening above σ_{xx}^c (solid red arrow). The inset in (b) illustrates the core softening of the effective intermolecular interaction $u^{2b}(R_{IJ})$ due to stress-induced molecular conformations at σ_{xx}^c (see Sec. III E). The images are for the same pair of representative molecules, each having stress state-dependent conformations. Molecular structures are superimposed on colored shapes to highlight and quantify conformer anisotropy $\lambda_x^2 : \lambda_z^2(I)$ as explained in the caption of Fig. 7.

with Eq. (13) with the instantaneous ρ_I computed accordingly to Eq. (12), in which ω_ρ is the Lucy function with the cutoff R_{cut} .

The forces $f^{2b}(R, V, T)$ and the potentials $u^{2b}(R, V, T)$ [Eq. (11)] are displayed in Fig. 6. During the elastic phase, the f^{2b} , u^{2b} profiles clearly show an increase in structure indicating the stiffening of the effective intermolecular interaction. This is followed by the softening of the $A(R^N, V, T)$ above σ_{xx}^c which is manifested in the nearly structureless $f^{2b}(R)$. Furthermore, as illustrated in the inset to Fig. 6(b), the $u^{2b}(R)$ [and therefore $f^{2b}(R)$] clearly exhibits a core softening [55] at σ_{xx}^c . A similar core softening is observed in the $u^{2b}(R)$ resulting from MSCG force matching to liquid, amorphous, and crystalline RDX systems hydrostatically compressed to pressures up to 20 GPa [52]. Systems with core-softened

interactions often show a rich spectrum of structural instabilities and phase transitions [56–59]. Moreover, the general result is that if the interaction potential has a certain degree of core softening, then it is likely that a novel phase transition may occur due to structural instabilities associated with the core collapse [96].

E. Shear banding as structural phase transition

We start the section with an analysis of the stress-induced changes in the population statistics of the molecular conformers observed in [100]-compressed s and S cells using the $f^{2b}(R)$ obtained in Sec. III D, an analysis similar to one performed in [52]. The analysis suggests that the core softening of the $f^{2b}(R)$, $u^{2b}(R)$ is caused by the abrupt increase in the number of molecular conformers with low and high sphericities, properties that are quantified using the set of molecular radius of gyration tensors $\{\hat{S}_I\}_{I=1}^N$ [97,98]. The \hat{S}_I is a 3×3 positive-definite matrix with principal values $\lambda_{I,x}^2 \leq \lambda_{I,y}^2 \leq \lambda_{I,z}^2$. We are particularly interested in the change of the molecular shape anisotropy which can be defined in terms of molecular (inverse) aspect ratio: $\lambda_x^2 : \lambda_z^2(I) \equiv \lambda_{I,x}^2 \lambda_{I,z}^{-2}$. A smaller $\lambda_x^2 : \lambda_z^2(I)$ indicates that the geometry of the I th molecule is close to planar (*eee* conformer). More spherical molecular conformations in which one or more NO_2 groups are bent toward the axial position (the *aaa*, *eee*, *aae* arrangements) have larger $\lambda_x^2 : \lambda_z^2(I)$. The behavior of $\lambda_x^2 : \lambda_z^2 \equiv E[\lambda_x^2 : \lambda_z^2(I)]$ vs σ_{xx} was analyzed in [52]. That analysis indicates that qualitatively, the $\lambda_x^2 : \lambda_z^2$ vs σ_{xx} dependencies for the s and S cells are very similar. In both cases, the $\lambda_x^2 : \lambda_z^2$ monotonically increases in the elastic regime, indicating a conformation change of the molecules from *aae* toward more spherical *aii* conformers. The max $\lambda_x^2 : \lambda_z^2$ is reached at a σ_{xx} somewhat below σ_{xx}^c when the intramolecular structures undergo abrupt changes in the whole s cell and in the S regions of the S cell, with approximately half of the conformers in the *aaa* state, and the other half in the *eee* state. Here, we perform a similar analysis using the $f^{2b}(R)$ obtained in Sec. III D. Deformation maps of molecules colored by the molecular aspect ratio of the s and S cells at selected σ_{xx} are presented in Fig. 7. At about $\sigma_{xx} = 5$ GPa in the S cell, the clusters of the *aaa* and *eee* conformers start to appear and localize within regions that eventually transform into shear bands. These clusters can be viewed as the nuclei of a unique structural S phase. The abrupt significant increase of the *aaa* and *eee* conformers leads to the core softening of the $u^{2b}(R)$ and hence of the $A(R^N, V, T)$ as illustrated in the inset to Fig. 6(b). This behavior underlies a structural phase transition associated with the shear banding, as indicated by the analysis of the $A(R^N, V, T)$ presented next.

Next, we calculated the isotherm $A(R^N, V, T)$ for the S cell [100]-compressed to σ_{xx} by integration of Eq. (15) using the final R^N in the NsT simulations. The corresponding Gibbs FE $G(\hat{\sigma}, T) = A + V\hat{\sigma} : \hat{\varepsilon}$ as a function of σ_{xx} is plotted in Fig. 8. The cusp at σ_{xx}^c indicates a first-order structural phase transition. The $G(\hat{\sigma}, T)$ is concave ($\partial^2 G / \partial \sigma_{xx}^2 \leq 0$) below and above σ_{xx}^c as expected for the structurally stable R^N . At σ_{xx}^c , the shear bands with the finite order parameter $\gamma = 0.48$ spontaneously appear. The γ monotonically increases as $\sigma_{xx} > \sigma_{xx}^c$ increases, indicating the shear localization in both P and S bands. Some interesting aspects of the effective

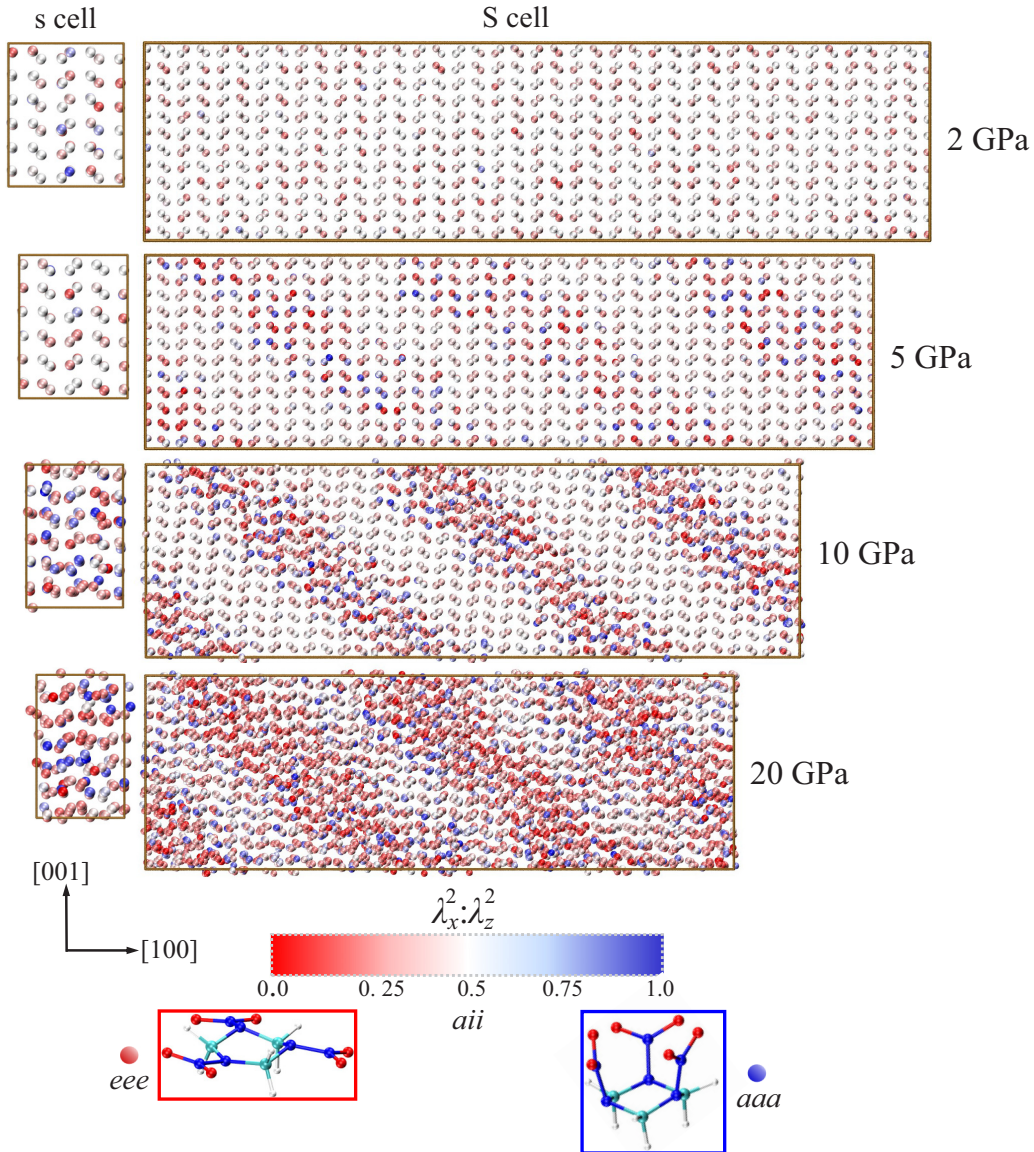


FIG. 7. Color map visualization of the molecular conformations in the s and S cells which are $[100]$ compressed to different σ_{xx} (values shown on the right). The spheres are locations of molecular c.m. (R^N lattice). The l th sphere is colored in accordance to the value of the molecular inverse aspect ratio $\lambda_x^2 : \lambda_z^2 (l)$ as indicated in the color-scale legend.

intermolecular interaction $u^{2b}(R_{IJ}, V, T)$ in the elastic region is illustrated by the potential $G(\hat{\sigma}, T) - A_0 = \sum_{I < J} u^{2b}(R_{IJ}, V, T) + V \hat{\sigma} : \hat{\varepsilon}$ in Fig. 8 [the potential A_0 is defined in Eq. (11)]. The potential $G(\hat{\sigma}, T) - A_0$ describes the integral value of the effective intermolecular forces and complements the data in Fig. 6. The energy $G(\hat{\sigma}, T) - A_0$ monotonically decreases in the elastic region 0–6 GPa, apparently due to the rapid increase in the effective attraction between molecules from the second coordination shell, $R_{IJ} > 8 \text{ \AA}$.

The first-order transition with incipient deformation twinning bands as transient microstructure is confirmed by analyzing the FE $\Delta A(\gamma)$ of an idealized S cell R^N at $\sigma_{xx} = 10 \text{ GPa}$ which has lamellar microstructure with homogeneous shear bands of various geometries. To prepare the S cell of

a target geometry, we first generated the lattice $R^N = \hat{F}^a R_0^N$ from the stress-free lattice R_0^N using the affine deformation $\hat{F}^a = a_\sigma a_0^{-1} \hat{n}_{[100]} \otimes \hat{n}_{[100]}$ where a_σ is the $[100]$ dimension of the cell in equilibrium at σ_{xx} . Next, we introduced localized simple shear deformation bands of the geometry $(L_S, L_P, \alpha, \gamma)$ into the uniform R^N . The R^N was then subjected to a simple shear $\hat{F}^p(\gamma) = \hat{I} + \gamma \hat{s} \otimes \hat{n}$ where $\hat{s} \cdot \hat{n}_{[100]} = \cos \alpha$ in the S regions (of width L_S) and to a complementary simple shear $\hat{F}^{p'}(\gamma) = \hat{I} - L_S L_P^{-1} \gamma \hat{s} \otimes \hat{n}$ within the P regions (of width L_P). The S bands are uniformly spaced by the P bands. Examples of the deformed cell with the S bands colored in pink are displayed in Fig. 9. The set of $\Delta A(\gamma)$ shown in Fig. 9(a) is for the geometry $L_S = 15 \text{ \AA}$, $L_S L_P^{-1} = 0.48$, $\alpha = 45^\circ$ which resembles the geometry of the S bands in the atomistically simulated S cell [Fig. 9(a)]. The $\Delta A(\gamma)$

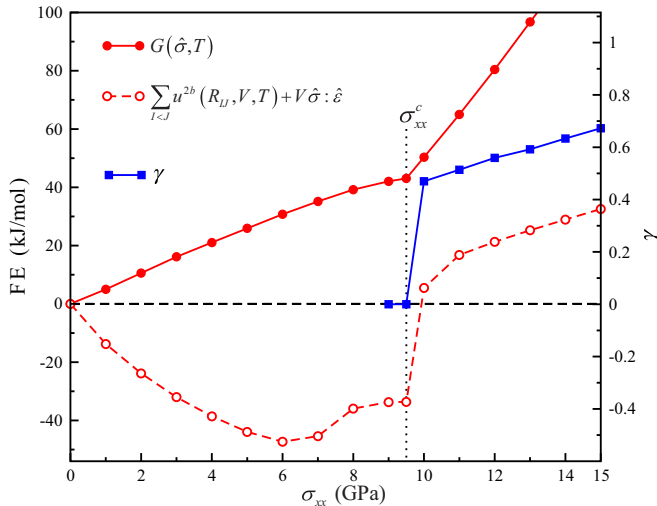


FIG. 8. (Left axis) Gibbs FE isotherm $G(\hat{\sigma}, T) = A + V\hat{\sigma} : \hat{\epsilon}$ with the Helmholtz FE A calculated using Eq. (15) (solid red, filled circles) and isotherm $\sum_{I<J} u^{2b}(R_{IJ}, V, T) + V\hat{\sigma} : \hat{\epsilon}$ (dashed, open circles) for the S cell [100] compressed to σ_{xx} . (Right axis) Corresponding isotherm for the order parameter $\gamma(R^N)$ (solid blue, squares).

curves vs σ_{xx} exhibit a generic behavior of the first-order GL model [31] as follows: (1) For each σ_{xx} , the $\Delta A(\gamma)$ is nonsymmetrical, pointing to the presence of the cubic term ΔA_{γ^3} and hence the existence of the first-order phase transition; (2) for $0 \leq \sigma_{xx} < 5$ GPa, the $\Delta A(\gamma)$ has one minimum which is the P phase and one inflection (in the generic GL model the inflection exists for $\Delta a \equiv \Delta A_{\gamma^2} \Delta A_{\gamma^4} \Delta A_{\gamma^3}^{-2} \geq \frac{9}{32}$); (3) at $\sigma_{xx} = 5$ GPa, the $\Delta A(\gamma)$ deviates from the generic GL model since an additional inflection appears, pointing to the influence of the $o(\gamma^4)$ terms in Eq. (18); (4) for $6 \leq \sigma_{xx} < 8$ GPa, the first inflection becomes a metastable minimum which is a sheared (martensitic twinnedlike) phase (the corresponding generic GL condition is $\frac{1}{4} < \Delta a < \frac{9}{32}$); (5) at $\sigma_{xx} = 8$ GPa, the metastable minimum at $\gamma = 0.55$ corresponding to the twinnedlike phase (which is close to the atomistic value of 0.48 in Fig. 8) becomes slightly more stable relative to the parent phase. The parent and twinnedlike phase minima are separated by an activation barrier. This is the condition for a first-order (discontinuous) phase transition (the generic GL condition is $\Delta a = \frac{1}{4}$). The lattice remains in the parent geometry as the necessary fluctuations to overcome the barrier are not available; (6) with a further increase in σ_{xx} , the stability of the sheared phase monotonically increases while the barrier separating the parent and sheared phases decreases ($0 < \Delta a < \frac{1}{4}$). The barrier eventually disappears at the yield stress σ_{xx}^c (10 GPa) with the $\gamma = 0.55$ state becoming the global minimum. This minimum corresponds to the spontaneously sheared (twinnedlike) lattice of the idealized laminate microstructures in Fig. 9. In the atomistic simulations, the amorphous band microstructure in R^N at σ_{xx}^c appears at smaller γ (~ 0.48) (Fig. 8). This is due to amorphization of the shear bands as the system jumps to a state with large γ for which the deformation twins cannot be accommodated or even may not exist as the $u^{2b}(R)$ is a function of γ . This points to the transient nature of the twinning microstructure in

α -RDX and characterizes the shear banding as a first-order transition.

Next, we calculated $\Delta A(\gamma)$ for geometries that significantly differ from the geometry used in Fig. 9(a), which are illustrated in Fig. 9(b). In the first family of curves, we used the same L_S, L_P (labeled as L_S^0, L_P^0) as in Fig. 9(a), but the angle α was varied (between 30° and 60°). In the second set of calculations, we doubled the bandwidth (labeled as L_S^1) with the corresponding L_P^1 selected to preserve the number of the bands (equal to three) while $\alpha = 45^\circ$. The results are shown in Fig. 9(b). For the (L_S^0, L_P^0) geometry, stable first-order twinning phase minima exist for both $\alpha = 30^\circ, 60^\circ$ but these states are less stable compared to the twinning state for $\alpha = 45^\circ$. With an increase in the bandwidth [(L_S^1, L_P^1) geometry], the twinning minimum quickly degenerates into an inflection point. $\alpha = 45^\circ$ and 135° are crystallographically equivalent directions and hence the crisscross pattern that is observed in the atomistic simulations can arise (Figs. 2 and 4). The ΔA_{γ^n} constants can be easily obtained by numerical differentiation of the $\Delta A(\gamma)$ and their comparison to the GL generic conditions [31] would indicate the importance of the $o(\gamma^4)$ terms. However, at this point we see that the generic GL model gives an excellent qualitative description of the stress-induced criticality in α -RDX.

The analysis presented here indicates that the nanoscale shear banding in α -RDX represents a first-order phase transition with the twinning phase being bypassed. This mechanism may be important in low-symmetry molecular crystals in which the deformation slip and twinning modes are characterized by a high activation energy [99]. The intrinsic structural instability leading to the phase transformation in the R^N lattice clearly correlates with the abrupt core softening of the u^{2b} [Fig. 6(b)]. The core softening transforms the $A(R^N, V, T)$ surface toward multiple characteristic scales, a feature which is known to cause structural phase transitions as well as thermodynamic anomalies [56]. Moreover, the core collapse of the intermolecular effective interaction is clearly caused by stress-induced molecular conformational changes prompting the conclusion that there is a hierarchy of structural instabilities involved with shear banding in α -RDX.

IV. CONCLUSIONS

We presented a formalism which couples the GL phenomenology with the CG (molecular c.m. projected) Helmholtz FE from bottom-up principles using the MSCG/FM method to study the plastic response of an energetic molecular crystal under quasistatic loading. Our microscopic theory indicates that transient bands of localized twinning strain triggered by the core softening (core collapse) of the effective intermolecular interaction $u^{2b}(R)$ could be a fundamental instability underlying a first-order phase transition associated with the plastic response in solids composed of structurally complex flexible molecules. Although we considered a specific energetic crystal polymorph (α -RDX), the proposed mechanism of nanoscale shear banding (which involves the transient localization of the twinning shear and criticality due to the stress-induced modification of the effective intermolecular interaction) might be applicable to a wider range of molecular

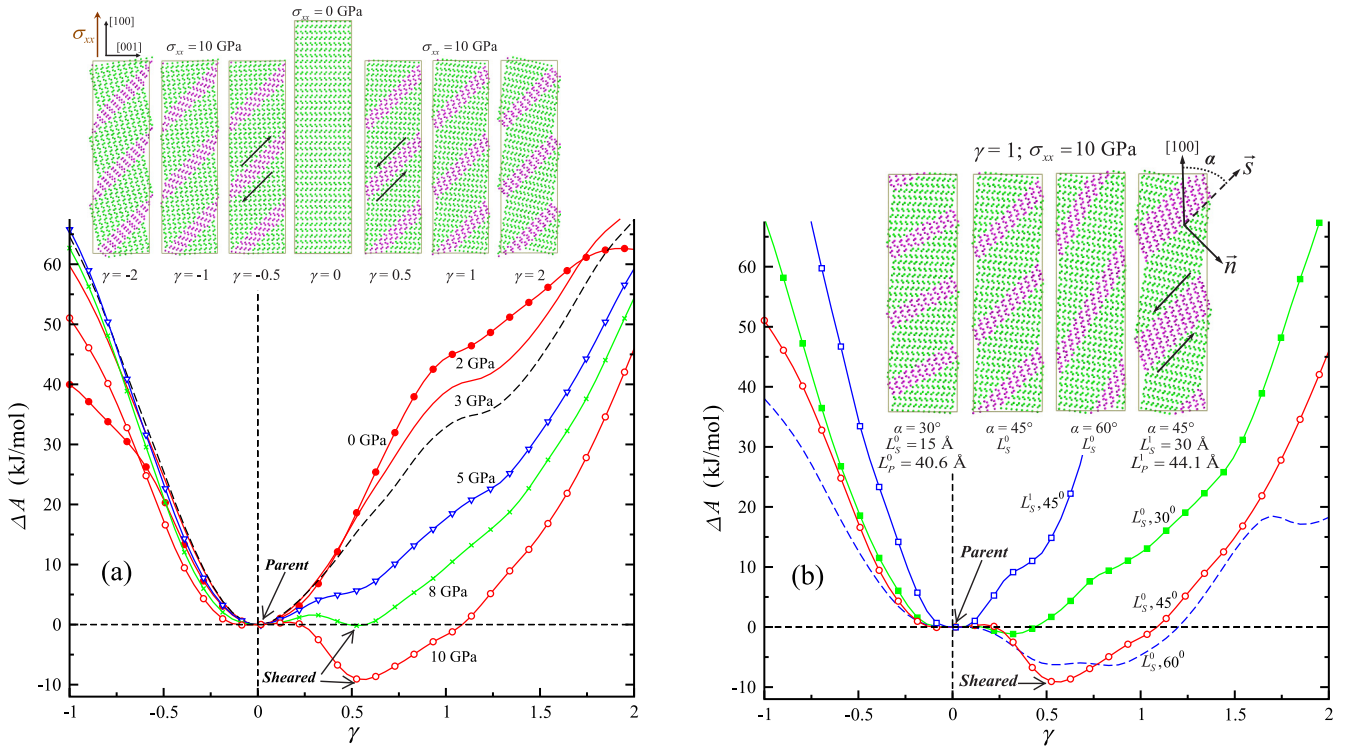


FIG. 9. Helmholtz FE $\Delta A(\gamma)$ as a function of the order parameter γ for localization of twinning strain in idealized laminate microstructures of various geometries $(L_S, L_P, \alpha, \gamma)$ in the S cell lattice R^N which is $[100]$ compressed to selected σ_{xx} . (a) The $\Delta A(\gamma)$ for the geometry $L_S = 15 \text{ \AA}$, $L_S L_P^{-1} = 0.48$ and $\alpha = 45^\circ$ which resembles the geometry of the shear bands from the atomistic simulation. The values of σ_{xx} label the $A(\gamma)$ curves. The parent ($\gamma = 0$) and sheared ($\gamma \neq 0$) phase minima are indicated in the $\sigma_{xx} = 8$ and 10 GPa curves by arrows. (b) The $A(\gamma)$ at $\sigma_{xx} = 10$ GPa and the geometries $(L_S^{0,1}, L_P^{0,1}, \alpha, \gamma)$ (as indicated in the legends). In both panels, insets visualize representative R^N configurations at $\sigma_{xx} = 10$ GPa used in the calculations, with the arrows indicating directions of shear.

crystals with a type of structural transformation underlying the plastic response determined by the crystal symmetry and FE landscape. In α -RDX, the clusters of the conformers (aaa , eee) that populate the shear bands emerge before the transition to plastic response. The clusters tend to localize within the regions which eventually transform into the incipient deformation twinning bands followed by the shear bands. These can be viewed as the nuclei of the unique structural phase, another indicator of the first-order phase transformation at the elastic-plastic transition. The core softening of the $u^{2b}(R)$ is linked to the growth of stress-induced conformational changes. In crystals with hard to activate deformation twinning modes such as α -RDX, the deformation twinninglike bands are expected to amorphize along a discontinuous structural transition. This constitutes an equilibrium mechanism for spontaneous nanoscale shear banding. In shock-compressed α -RDX, the instabilities may

contribute to the onset of plastic strain localization followed by shock energy dissipation and thermal softening effects within the spontaneously formed amorphous shear bands. On the methodological side, the proposed formalism may have far-reaching applications due to its ability to study structural phase transitions in real molecular crystals, a challenge for conventional methods based on model FE functionals of a few order parameters [100].

ACKNOWLEDGMENTS

The authors wish to thank Dr. Patrick G. Lafond, Dr. John K. Brennan, Dr. James P. Larentzos, and Dr. Brian C. Barnes of the U.S. Army DEVCOM Army Research Laboratory for helpful comments. This work was supported in part by high-performance computer time and resources from the DoD High Performance Computing Modernization Program.

- [1] M. A. Meyers, V. F. Nesterenko, J. C. LaSalvia, and Q. Xue, *Mater. Sci. Eng.: A* **317**, 204 (2001).
- [2] T. Z. Blazynski (Ed.), *Materials at High Strain Rates* (Elsevier Applied Science Publishers, London, 1987).
- [3] B. L. Holian and P. S. Lomdahl, *Science* **280**, 2085 (1998).

- [4] J. J. Rimoli, E. Gurses, and M. Ortiz, *Phys. Rev. B* **81**, 014112 (2010).
- [5] E. Jaramillo, T. D. Sewell, and A. Strachan, *Phys. Rev. B* **76**, 064112 (2007).
- [6] R. A. Austin, N. R. Barton, J. E. Reaugh, and L. E. Fried, *J. Appl. Phys.* **117**, 185902 (2015).

- [7] V. I. Levitas and R. Ravelo, *Proc. Natl. Acad. Sci. USA* **109**, 13204 (2012).
- [8] S. Kartha, J. A. Krumhansl, J. P. Sethna, and L. K. Wickham, *Phys. Rev. B* **52**, 803 (1995).
- [9] A. Saxena, Y. Wu, T. Lookman, S. R. Shenoy, and A. R. Bishop, *Phys. A (Amsterdam)* **239**, 18 (1997).
- [10] M. Ortiz and E. A. Repetto, *J. Mech. Phys. Solids* **47**, 397 (1999).
- [11] M. P. Kroonblawd and L. E. Fried, *Phys. Rev. Lett.* **124**, 206002 (2020).
- [12] P. Lafourcade, C. Denoual, and J. B. Maillat, *J. Phys. Chem. C* **122**, 14954 (2018).
- [13] P. Lafourcade, C. Denoual, and J. B. Maillat, *Phys. Rev. Mater.* **3**, 053610 (2019).
- [14] C. S. Coffey and J. Sharma, *J. Appl. Phys.* **89**, 4797 (2001).
- [15] B. Dodd and Y. Bai (Eds.), *Adiabatic Shear Localization: Frontiers and Advances* (Elsevier, Boston, 2012).
- [16] J. S. Langer, *Phys. Rev. E* **95**, 013004 (2017).
- [17] J. Frenkel and T. Kontorova, *J. Phys.-USSR* **1**, 137 (1939).
- [18] V. I. Levitas and D. L. Preston, *Phys. Rev. B* **66**, 134206 (2002).
- [19] G. P. Zheng and M. Li, *Phys. Rev. B* **80**, 104201 (2009).
- [20] Y. Z. Wang and J. Li, *Acta Mater.* **58**, 1212 (2010).
- [21] F. E. Hildebrand and C. Miehe, *Philos. Mag.* **92**, 4250 (2012).
- [22] S. Rudraraju, A. Van der Ven, and K. Garikipati, *npj Comput. Mater.* **2**, 16012 (2016).
- [23] G. Parisi, I. Procaccia, C. Rainone, and M. Singh, *Proc. Natl. Acad. Sci. USA* **114**, 5577 (2017).
- [24] D. Richard, M. Ozawa, S. Patinet, E. Stanifer, B. Shang, S. A. Ridout, B. Xu, G. Zhang, P. K. Morse, J. L. Barrat, L. Berthier, M. L. Falk, P. Guan, A. J. Liu, K. Martens, S. Sastry, D. Vandembroucq, E. Lerner, and M. L. Manning, *Phys. Rev. Mater.* **4**, 113609 (2020).
- [25] J. L. Ericksen, *Arch. Ration. Mech. Anal.* **72**, 1 (1979).
- [26] L. Lei and M. Koslowski, *Philos. Mag.* **91**, 865 (2011).
- [27] S. K. Park and Y. Diao, *Chem. Soc. Rev.* **49**, 8287 (2020).
- [28] J. S. Langer and K. C. Le, *Proc. Natl. Acad. Sci. USA* **117**, 29431 (2020).
- [29] M. L. Falk and J. S. Langer, *Phys. Rev. E* **57**, 7192 (1998).
- [30] S. Kartha, T. Castan, J. A. Krumhansl, and J. P. Sethna, *Phys. Rev. Lett.* **67**, 3630 (1991).
- [31] J. A. Krumhansl and R. J. Gooding, *Phys. Rev. B* **39**, 3047 (1989).
- [32] L. D. Landau and D. Ter-Haar, *Collected Papers of L. D. Landau* (Pergamon Press, Oxford, 1965).
- [33] N. Provatas and K. Elder, *Phase-Field Methods in Materials Science and Engineering* (Wiley-VCH, Singapore, 2010).
- [34] V. I. Levitas, V. A. Levin, K. M. Zingerman, and E. I. Freiman, *Phys. Rev. Lett.* **103**, 025702 (2009).
- [35] J. Y. Cho, A. V. Idesman, V. I. Levitas, and T. Park, *Int. J. Solids Struct.* **49**, 1973 (2012).
- [36] V. I. Levitas, *Int. J. Plast.* **49**, 85 (2013).
- [37] V. I. Levitas, *Acta Mater.* **61**, 4305 (2013).
- [38] V. I. Levitas, H. Chen, and L. M. Xiong, *Phys. Rev. B* **96**, 054118 (2017).
- [39] H. Emmerich, H. Lowen, R. Wittkowski, T. Gruhn, G. I. Toth, G. Tegze, and L. Granasy, *Adv. Phys.* **61**, 665 (2012).
- [40] R. J. Asaro and J. R. Rice, *J. Mech. Phys. Solids* **25**, 309 (1977).
- [41] M. Homayonifar and J. Mosler, *Int. J. Plast.* **27**, 983 (2011).
- [42] E. Darve, D. Rodriguez-Gomez, and A. Pohorille, *J. Chem. Phys.* **128**, 144120 (2008).
- [43] M. Sprik and G. Ciccotti, *J. Chem. Phys.* **109**, 7737 (1998).
- [44] W. G. Noid, *J. Chem. Phys.* **139**, 090901 (2013).
- [45] T. V. Ramakrishnan and M. Yussouff, *Phys. Rev. B* **19**, 2775 (1979).
- [46] S. Angioletti-Uberti, M. Ceriotti, P. D. Lee, and M. W. Finnis, *Phys. Rev. B* **81**, 125416 (2010).
- [47] L. Y. Lu and G. A. Voth, *J. Chem. Phys.* **134**, 224107 (2011).
- [48] S. Izvekov and G. A. Voth, *J. Phys. Chem. B* **109**, 2469 (2005).
- [49] W. G. Noid, J. W. Chu, G. S. Ayton, V. Krishna, S. Izvekov, G. A. Voth, A. Das, and H. C. Andersen, *J. Chem. Phys.* **128**, 244114 (2008).
- [50] S. Izvekov, P. W. Chung, and B. M. Rice, *J. Chem. Phys.* **133**, 064109 (2010).
- [51] J. D. Moore, B. C. Barnes, S. Izvekov, M. Lisal, M. S. Sellers, D. E. Taylor, and J. K. Brennan, *J. Chem. Phys.* **144**, 104501 (2016).
- [52] S. Izvekov and B. M. Rice, *J. Chem. Phys.* **155**, 064503 (2021).
- [53] J. W. Christian and S. Mahajan, *Prog. Mater. Sci.* **39**, 1 (1995).
- [54] P. C. Hemmer and G. Stell, *Phys. Rev. Lett.* **24**, 1284 (1970).
- [55] G. Stell and P. C. Hemmer, *J. Chem. Phys.* **56**, 4274 (1972).
- [56] P. Vilaseca and G. Franzese, *J. Non-Cryst. Solids* **357**, 419 (2011).
- [57] P. C. Hemmer, E. Velasco, L. Mederos, G. Navascues, and G. Stell, *J. Chem. Phys.* **114**, 2268 (2001).
- [58] J. M. Kincaid, G. Stell, and C. K. Hall, *J. Chem. Phys.* **65**, 2161 (1976).
- [59] S. Izvekov, N. S. Weingarten, and E. F. C. Byrd, *J. Chem. Phys.* **148**, 094504 (2018).
- [60] W. Greiner, *Classical Mechanics: Systems of Particles and Hamiltonian Dynamics*, 2nd ed. (Springer, Berlin, 2010).
- [61] S. Izvekov and G. A. Voth, *J. Chem. Phys.* **123**, 134105 (2005).
- [62] C. Hijón, P. Espanol, E. Vanden-Eijnden, and R. Delgado-Buscalioni, *Faraday Discuss.* **144**, 301 (2010).
- [63] S. Izvekov, *J. Chem. Phys.* **138**, 134106 (2013).
- [64] S. Izvekov, *Phys. Rev. E* **104**, 024121 (2021).
- [65] A. Das and H. C. Andersen, *J. Chem. Phys.* **132**, 164106 (2010).
- [66] S. Izvekov, P. W. Chung, and B. M. Rice, *J. Chem. Phys.* **135**, 044112 (2011).
- [67] T. Sanyal and M. S. Shell, *J. Chem. Phys.* **145**, 034109 (2016).
- [68] P. B. Warren, *Phys. Rev. E* **68**, 066702 (2003).
- [69] R. J. Hardy, *J. Chem. Phys.* **76**, 622 (1982).
- [70] J. F. Lutsko, *J. Appl. Phys.* **64**, 1152 (1988).
- [71] S. Nose, *J. Chem. Phys.* **81**, 511 (1984).
- [72] S. Melchionna, G. Ciccotti, and B. L. Holian, *Mol. Phys.* **78**, 533 (1993).
- [73] D. I. A. Millar, I. D. H. Oswald, D. J. Francis, W. G. Marshall, C. R. Pulham, and A. S. Cumming, *Chem. Commun.* **5**, 562 (2009).
- [74] S. Izvekov, J. P. Larentzos, J. K. Brennan, and B. M. Rice, *J. Mater. Sci.* **57**, 10627 (2022).
- [75] R. J. Karpowicz and T. B. Brill, *J. Phys. Chem.* **88**, 348 (1984).
- [76] I. F. Shishkov, L. V. Vilkov, M. Kolonits, and B. Rozsondai, *Struct. Chem.* **2**, 57 (1991).
- [77] N. J. Harris and K. Lammertsma, *J. Am. Chem. Soc.* **119**, 6583 (1997).

- [78] B. M. Rice and C. F. Chabalowski, *J. Phys. Chem. A* **101**, 8720 (1997).
- [79] T. Vladimiroff and B. M. Rice, *J. Phys. Chem. A* **106**, 10437 (2002).
- [80] R. Infante-Castillo, L. C. Pacheco-Londono, and S. P. Hernandez-Rivera, *J. Mol. Struct.* **970**, 51 (2010).
- [81] N. Mathew and R. C. Picu, *J. Chem. Phys.* **135**, 024510 (2011).
- [82] H. G. Gallagher, P. J. Halfpenny, J. C. Miller, and J. N. Sherwood, *Philos. Trans. R. Soc. London, Ser. A* **339**, 293 (1992).
- [83] K. J. Ramos, D. E. Hooks, and D. F. Bahr, *Philos. Mag.* **89**, 2381 (2009).
- [84] L. B. Munday, S. D. Solares, and P. W. Chung, *Philos. Mag.* **92**, 3036 (2012).
- [85] J. D. Clayton and R. Becker, *J. Appl. Phys.* **111**, 063512 (2012).
- [86] J. Liu, Q. Zeng, Y. L. Zhang, and C. Y. Zhang, *J. Phys. Chem. C* **120**, 15198 (2016).
- [87] G. D. Smith and R. K. Bharadwaj, *J. Phys. Chem. B* **103**, 3570 (1999).
- [88] D. Bedrov, C. Ayyagari, G. D. Smith, T. D. Sewell, R. Menikoff, and J. M. Zaug, *J. Comput-Aided Mater. Des.* **8**, 77 (2002).
- [89] L. Q. Zheng and D. L. Thompson, *J. Chem. Phys.* **125**, 084505 (2006).
- [90] D. Bedrov, J. B. Hooper, G. D. Smith, and T. D. Sewell, *J. Chem. Phys.* **131**, 034712 (2009).
- [91] L. B. Munday, P. W. Chung, B. M. Rice, and S. D. Solares, *J. Phys. Chem. B* **115**, 4378 (2011).
- [92] F. L. Addessio, D. J. Luscher, M. J. Cawkwell, and K. J. Ramos, *J. Appl. Phys.* **121**, 185902 (2017).
- [93] M. J. Cawkwell, T. D. Sewell, L. Q. Zheng, and D. L. Thompson, *Phys. Rev. B* **78**, 014107 (2008).
- [94] A. Higginbotham, M. J. Suggit, E. M. Bringa, P. Erhart, J. A. Hawreliak, G. Mogni, N. Park, B. A. Remington, and J. S. Wark, *Phys. Rev. B* **88**, 104105 (2013).
- [95] J. Clayton, *J. Mater. Sci.* **53**, 5515 (2018).
- [96] A. Scala, M. R. Sadr-Lahijany, N. Giovambattista, S. V. Buldyrev, and H. E. Stanley, *J. Stat. Phys.* **100**, 97 (2000).
- [97] D. N. Theodorou and U. W. Suter, *Macromolecules* **18**, 1206 (1985).
- [98] H. Arkin and W. Janke, *J. Chem. Phys.* **138**, 054904 (2013).
- [99] R. W. Armstrong and W. L. Elban, in *Dislocations in Solids*, edited by F. R. N. Nabarro and J. P. Hirth (Elsevier, Amsterdam, 2004), p. 403.
- [100] K. R. Elder and M. Grant, *Phys. Rev. E* **70**, 051605 (2004).